ELSEVIER

Contents lists available at ScienceDirect

# Construction and Building Materials

journal homepage: www.elsevier.com/locate/conbuildmat





# Monitoring restrained shrinkage and cracks of ultra-high-performance concrete (UHPC) using distributed fiber optic sensors

Xiao Tan<sup>a</sup>, Jiang Du<sup>a</sup>, Qinghua Zhang<sup>b</sup>, Weina Meng<sup>a</sup>, Yi Bao<sup>a,\*</sup>

- <sup>a</sup> Department of Civil. Environmental and Ocean Engineering. Stevens Institute of Technology. Hoboken. N.I. United States
- <sup>b</sup> School of Civil Engineering, Southwest Jiaotong University, Chengdu, Sichuan, China

### ARTICLE INFO

Keywords:
Concrete cracking
Distributed fiber optic sensor (DFOS)
Early-age shrinkage
Optical Frequency Domain Reflectometry
(OFDR)
Restrained shrinkage
Ultra-high-performance concrete (UHPC)

### ABSTRACT

This paper presents a method to measure the shrinkage and cracks of ultra-high-performance concrete (UHPC) using distributed fiber optic sensors. UHPC prisms and rings were prepared and instrumented with fiber optic cables which served as distributed sensors to assess restrained shrinkage based on the Optical Frequency Domain Reflectometry (OFDR) technology with a 0.65-millimeter resolution. The initiation and development of shrinkage cracks were detected, located, quantified, and visualized from the strain distributions. The effect of steel fibers, lightweight sand, and shrinkage reducing agent on shrinkage distribution and crack pattern was investigated. The results indicate that the restrained shrinkage of UHPC decreased from  $809~\mu e$  to  $245~\mu e$  by using steel fibers, lightweight sand, and shrinkage reduce agent. The maximum crack width decreased from 1.605~mm to 0.065~mm. This research enhances the capability of monitoring shrinkage and cracks and supports the development of low-shrinkage UHPC.

## 1. Introduction

Cracking in concrete is one of the most important causes of the degradation of civil structures. Throughout the lifespan of a concrete structure, there are many possible causes of cracking, such as overload [1], collision [2], earthquake [3], and early-age shrinkage [4]. Shrinkage is an intrinsic dimension reduction of a material. Most of the shrinkage deformation of a concrete occurs at the early age before the concrete gains sufficient cracking resistance. Under a restrained condition, shrinkage often causes cracking and delamination [5], which provide new pathways for the ingress of harmful species such as sodium chloride, water, oxygen, and carbon dioxide, thus accelerating corrosion of steel bars embedded in concrete [6]. Steel corrosion produces expansive products that further aggravate the cracking in concrete. Even if concrete is not cracked due to shrinkage, shrinkage will cause residual stresses, which increase the possibility of cracking under operation loads. Cracks and delamination induced by the shrinkage of concrete adversely affect the safety and durability of structures from an early stage and throughout the entire life span. It is significant to mitigate and monitor the shrinkage and cracking of concrete.

The existing methods for mitigating shrinkage cracks can be categorized into three groups: (1) Enhance the crack resistance of concrete.

A representative method is to use chopped fibers that are dispersed in the matrix of concrete to bridge cracks. Various high-performance fiber-reinforced cementitious composites have been developed, such as ultra-high-performance concrete (UHPC) [7] and strain-hardening cementitious composite [8]. Following the same concept as the use of chopped fibers, nanomaterials have been used to further enhance the crack resistance of concrete [9]. (2) Reduce the shrinkage of concrete. Different methods have been developed to reduce the shrinkage by modifying the composition and processing of concrete. For instance, lightweight sand has been used as an internal curing agent to mitigate shrinkage [10]. (3) Seamlessly integrate the above two strategies. Chopped steel fibers and lightweight sand have been used to prepare UHPC that achieved high cracking resistance and low shrinkage [11].

Various methods have been developed to predict the shrinkage of concrete [12–17], and they have shown good performance in the laboratory. However, it is difficult to predict the shrinkage of concrete accurately in field applications because there are many factors that influence shrinkage, such as temperature, relatively humidity, and mechanical loads. To assess concrete shrinkage in the field, nondestructive evaluation (NDE) and structural health monitoring (SHM) technologies have been developed. Sound wave-based NDE techniques such as ultrasonic testing were applied to evaluate autogenous shrinkage [18],

E-mail address: yi.bao@stevens.edu (Y. Bao).

<sup>\*</sup> Corresponding author.

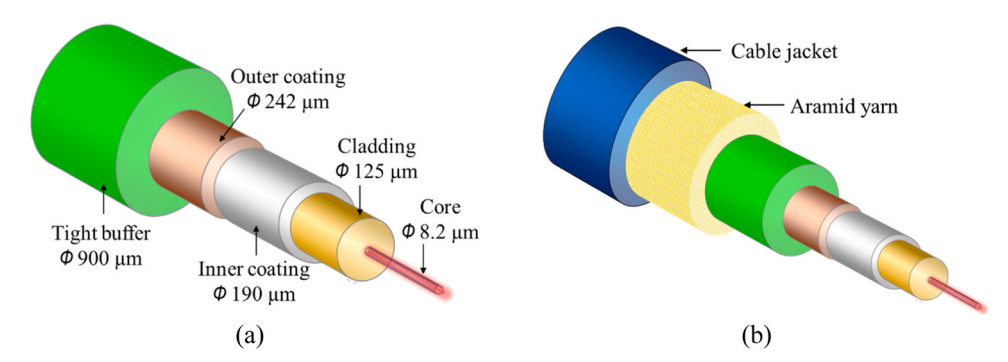


Fig. 1. Structures of the adopted fiber optic cables [49]: (a) tight coated fiber optic cable for measuring strains; and (b) fiber optic cable free of strains for measuring temperatures.

and acoustic emission techniques were used to detect and classify concrete cracking events [19,20]. However, it is generally difficult to use NDE techniques to assess internal shrinkage and cracks in concrete since concrete has heterogenous microstructures, due to the various sizes of aggregates and pores, which cause scatterings of the waves during their propagation, making the signal noisy and hard to interpret. To address this challenge, various in-situ sensors, such as dial gauges [21], strain gauges [22], vibrating wire strain sensors [23], and fiber Bragg grating sensors [24], have been used to monitor shrinkage. One of the major drawbacks is that each sensor monitors a local spot. In civil structures, many sensors must be installed at different locations, increasing the costs associated with sensors and sensor installation, extended construction time, and difficulties in the operation and the maintenance of the sensor system.

To address the challenges, distributed fiber optic sensors (DFOSs) have been proposed as an alternative method to monitor shrinkage [25] and cracking/delamination [26]. DFOS has a unique advantage of utilizing a single fiber optic cable as both the transmission line and the sensor with thousands of sensing points without sophisticated treatment [27,28]. Compared with other traditional sensors. DFOS has shown various advantages, such as distributed measurement and low sensor cost [29], and thus has been applied to the monitoring and assessment of large-scale civil structures, such as bridges [30], tunnels [31], pipelines [32], railways [33], and dams [34]. The performance of distributed sensors has been verified for various anomalies in laboratory tests [35-40] and field applications [41-44]. Previous research mainly focused on utilizing DFOS to measure shrinkage strain distributions of cement mortar [45] and conventional concrete [46,47]. For example, Bao et al. used distributed fiber optic sensors to measure the autogenous shrinkage of cement mortar based on pulse pre-pump Brillouin Optical Time Domain Analysis [45]. The sensors measured the shrinkage of mortar with a spatial resolution of 20 mm and detected a crack in a corrugated tube specimen. It was found that the shrinkage was nonuniform along the length of the specimen. The current practices use an average strain to represent shrinkage and cannot consider the nonuniform shrinkage.

Another important problem is related to the boundary conditions. Measuring shrinkage from tubes or prisms free to deform is useful for characterizing shrinkage at a material scale, but it is noted that concrete is often subject to restraints in realistic civil structures. To assess the restrained shrinkage of concrete, ring specimens recommended in AASHTO code [48] have been adopted, but it is difficult to evaluate the restrained shrinkage of UHPC using ring specimens because UHPC exhibits dense microcracks, which are difficult to identify and monitor from ring specimens. This challenge motivates the use of distributed fiber optic sensors to monitor restrained shrinkage of UHPC. Currently, there is lack of research on measuring restrained shrinkage and cracks induced by shrinkage using distributed sensors. Two important questions should be answered: (1) What are the methods to deploy distributed sensors for measuring the restrained shrinkage of UHPC? The

feasibility and performance of distributed sensors for measuring restrained shrinkage and cracks of UHPC is still unknown. (2) What are the methods to process and interpret the distributed sensor data for assessing restrained shrinkage? Existing studies on measuring restrained shrinkage using DFOS are limited to shrinkage detection and localization using off-specification specimens [46,47]. Research on quantitative evaluation and visualization of restrained shrinkage and crack of concrete is very rare.

The overarching goal of study research is to develop an in-situ monitoring method to directly measure the restrained shrinkage of UHPC and to detect, locate, quantify, and visualize shrinkage cracks using distributed fiber optic sensors. Specifically, this study has three main objectives: (1) Investigate the performance of a distributed fiber optic sensing technology with a high resolution (0.65 mm) for measuring restrained shrinkage and cracks. (2) Develop a method that utilizes strain distributions to locate, quantify, and visualize shrinkage cracks. (3) Investigate the initiation and development of shrinkage cracks when chopped fibers, lightweight sand, and shrinkage reducing agent are used. To this end, laboratory tests have been conducted using prism and ring specimens instrumented with distributed sensors. The specimens were utilized to investigate autogenous shrinkage and restrained shrinkage, respectively. Strain distributions were measured from the distributed sensors based on the Optical Frequency Domain Reflectometry (OFDR) method. The strain distributions were utilized to locate, quantify, and visualize the shrinkage and cracks of UHPC ring specimens.

This research has three novelties: (1) A new method is presented to monitor the initiation and the development of restrained shrinkage and the shrinkage-induced cracks of UHPC directly, and the location and severity of the cracks can be monitored in real time. This is different from and better than the current method: Attach strain gauges to the surface of steel rings to indirectly evaluate the cracking of concrete based on the sudden change of strain values. The conventional method is able to evaluate the cracking of conventional concrete which is brittle in tension and exhibits a single major crack. However, the conventional method is unable to evaluate the cracking of UHPC because UHPC can carry sustained load after cracks are generated in UHPC matrix. This post-cracking attribute of UHPC introduces challenges in evaluating the restrained shrinkage because the strain values measured from the strain gauges do not show a sudden change, different from the case of conventional concrete. In this sense, this research developed an important method which can be utilized to fill this technological gap. (2) The adopted sensor technology is different from previous research. This research adopted the OFDR technology to achieve high resolution (0.65 mm), which enables us to directly investigate the cracks within UHPC. (3) Based on the monitoring method, an integrated strategy is developed to mitigate shrinkage cracks for UHPC. The strategy supports the development of low-shrinkage or even shrinkage-crack-free UHPC, which helps further extend the service life and enhance the durability of concrete structures.

The remainder of the paper is structured as follows: Section 2 briefly introduces fiber optic cables and the sensing principle; Section 3 presents the experimental program conducted using UHPC prisms and rings; Section 4 analyzes and discusses the experimental results; and Section 5 summarizes the new findings obtained from this study.

## 2. Sensing principle

## 2.1. Fiber optic cables

In this study, two types of telecommunication-grade single-mode fiber optic cables packaged with polymeric coatings were employed as distributed fiber optic sensors, because those cables are commercially available, cost-effective, and sufficiently rugged for real construction applications. The structures of two types of fiber optic cables are shown in Fig. 1.

Fig. 1(a) shows the structure of the fiber optic cable for measuring strains. The fiber optic cable is composed of a fused silica core (diameter: 8.2 μm), a fused silica cladding (diameter: 125 μm), an inner polymeric coating (diameter: 190 µm), an outer polymeric coating (diameter: 242 μm), and a tight polymeric buffer (diameter: 900 μm). The sensing part is the fused silica core and cladding. Light waves propagate along the fiber optic cable through total internal reflection at the core-cladding interface. The inner coating is a soft acrylic layer which acts as a cushion agent and protects the fragile fiber core and cladding from being fractured under impact loads. The outer coating is a stiff acrylic layer which provides abrasion resistance. The elastic moduli of the fused silica fiber, inner coating, and outer coating are 72 GPa, 0.6 MPa, and 2 MPa, respectively. The tight buffer provides additional mechanical protection and makes it easier to operate the fiber in practice. Previous research indicates that the packaged fiber optic cables successfully survived the processes of fiber installation and concrete casting [44].

The fiber optic cable for temperature measurement was composed of a fiber optic strain cable, a layer of aramid yarn, and a cable jacket, as shown in Fig. 1(b). The aramid yarn is made from Kevlar $\mathbb R$ , which is crimped to the cable jacket after assembly. Therefore, any stress applied to the cable is carried by the aramid yarn instead of the fused silica fiber. In this way, the fiber optic cable is insensitive to mechanical strains but sensitive to temperature. Finally, an outer jacket (typically a 2-mm soft plastic material) surrounds the yarn and buffered fiber for a final layer of protection.

## 2.2. Optical frequency domain reflectometry

Rayleigh scattering in a fiber optic cable is an elastic scattering phenomenon that occurs when transmitted light interacts with the irregular microstructure of the fused silica [50]. The occurrence of irregularities can be attributed to the fabrication process of fiber optic cables. The irregularities have sizes comparable with the wavelength of light waves, leading to changes in the refractive index and the density of fiber core. OFDR measures temperature and strain changes by utilizing Rayleigh scattering in two different states [51], which are the reference state and the perturbed state. A light wave is transmitted into the core of a fiber optic cable, resulting in Rayleigh scattering. The backscattered signal is measured along the length of the fiber optic cable, and at each length along the fiber optic cable, the amplitude-wavelength data is converted into intensity-frequency data via Fast Fourier Transform. A cross-correlation operation is performed to compare the backscattered signals in the reference and perturbed states. The frequency shift is used to determine the strain and temperature. The distance of a scattering event is determined based on the travel time of the backscattered light wave. In this study, a data acquisition system (model: Luna ODiSi 6120) was utilized to conduct the measurement based on OFDR. The manufacturer-specified accuracies for strain and temperature are 5  $\mu\epsilon$ and 0.9 °C, respectively [52]. The frequency shift observed in the measurements is associated with changes in strain and temperature:

**Table 1**Concrete mix proportions and fresh properties (Unit: kg/m³).

Designation	M1	M2	М3	M4
Type I Portland cement	468.4	459.0	459.0	459.0
Finely-grounded slag	646.8	633.9	633.9	633.9
Shrinkage reducing agent	-	-	-	22.9
Lightweight sand	-	-	327.9	327.9
River sand	985.1	965.4	482.7	482.7
High-range water reducer (HRWR)	10.1	9.8	6.0	6.0
Water	249.9	244.8	247.0	247.0
Steel fibers	-	156	156	156

$$\frac{\Delta \lambda}{\lambda} = \frac{\Delta v}{v} = K_T T + K_\varepsilon \varepsilon \tag{1}$$

where  $\lambda$  and v refer to the mean optical wavelength and frequency, respectively;  $K_T$  and  $K_\varepsilon$  refer to the temperature and strain calibration coefficients, respectively.

The values of  $K_T$  and  $K_\varepsilon$  were experimentally calibrated as -0.15 GHz/°C and -1.46 GHz/ $\mu\epsilon$  [39], respectively. The temperature sensitivity coefficient ( $K_T$ ) was calibrated via tests using an electric furnace while the distributed sensor was free of strain. The test method is elaborated in reference [50]. The strain sensitivity coefficient ( $K_\varepsilon$ ) was calibrated via uniaxial tensile tests using a load frame at a constant room temperature. The test method is elaborated in reference [35].

## 3. Experimental program

## 3.1. Materials and mixture design

Four concrete mixtures with a low water-to-binder ratio were tested (Table 1), including a reference mixture (M1) and three UHPC mixtures (M2, M3, and M4). The mixtures were obtained from previous research [53]. The cement content is lower than typical UHPC mixtures, aiming to reduce cost and carbon footprint [53]. Cement was partially replaced by the finely-grounded slag. Compared with typical UHPC mixtures, the investigated UHPC mixtures achieved comparable mechanical properties and lower shrinkage, as elaborated in Sections 4.1 and 4.2.

Type I Portland cement (source: New Jersey Portland Cement Co.) and finely-grounded slag (source: Essex Cement Company LLC) were used as the binder. The water-to-binder ratio was 0.23. Two types of sand (i.e., river sand and lightweight sand) were used as fine aggregates. The river sand was provided by Whibco Corporation. The lightweight sand (source: Northeast Solite Corporation) was used as the internal curing agent. The water absorption value of the lightweight sand after soaking in water for 24 hours was 17.1%. The particle size distributions of the cement, slag, river sand, and lightweight sand are shown in Fig. 2. The chemical compositions were shown in Table 2.

To improve workability, a polycarboxylate-based high-range water reducer (HRWR) was used. The HRWR had a solid content of 34.4% and a specific gravity of 1.05, respectively. A shrinkage-reducing agent (manufacturer: Euclid Chemical) with amphiphilic low-molecular-weight polyether was used to decrease the shrinkage of UHPC. Straight steel fibers with a diameter of 0.2 mm and a length of 13 mm were incorporated to enhance the crack resistance. The tensile strength and elastic modulus of the steel fiber were 1.9 GPa and 203 GPa, respectively.

# 3.2. Specimens and investigated cases

Two types of specimens were prepared and tested, which are prism specimens for evaluating autogenous shrinkage in accordance with ASTM C157 [54] and ring specimens for evaluating restrained shrinkage in accordance with AASHTO T 334–08 [48]. The two types of specimens are depicted in Fig. 3. The prism specimens measured 25 mm  $\times$  25 mm  $\times$  280 mm. Each ring specimen was composed of a concrete ring and a

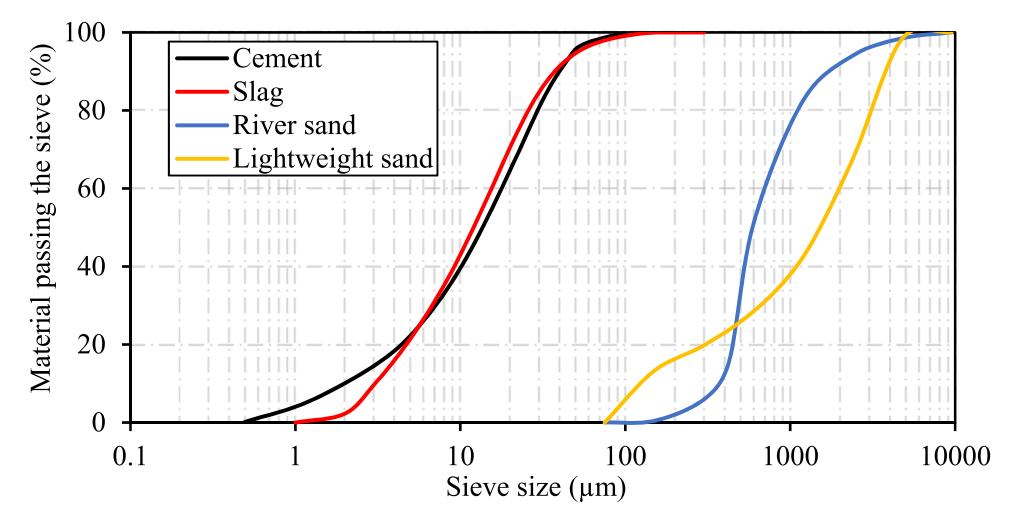
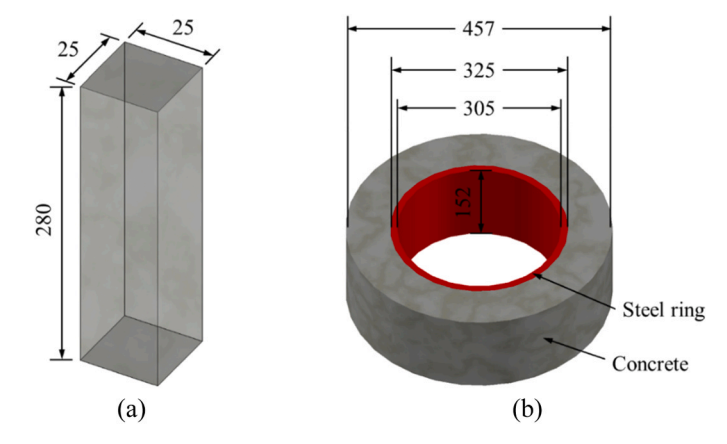


Fig. 2. Particle size distribution of Type I Portland cement, grounded slag, and lightweight sand.

 Table 2

 Chemical and physical properties of raw materials.

Chemical composition	Type I Portland cement	Finely- grounded slag	River sand	Lightweight sand
SiO <sub>2</sub> (%)	22.44	36.21	86.50	57.60
Al <sub>2</sub> O <sub>3</sub> (%)	2.76	11.10	0.39	19.40
Fe <sub>2</sub> O <sub>3</sub> (%)	2.24	0.76	1.47	9.60
CaO (%)	68.05	43.75	9.42	3.40
MgO (%)	0.91	5.09	-	2.60
SO <sub>3</sub> (%)	2.25	2.21	-	0.60
Na <sub>2</sub> O (%)	0.19	0.23	-	5.60
K <sub>2</sub> O (%)	0.11	0.40	-	-
TiO <sub>2</sub> (%)	0.14	0.58	-	-
P <sub>2</sub> O <sub>5</sub> (%)	0.09	0.02	-	-
Mn <sub>2</sub> O <sub>3</sub> (%)	0.03	0.36	-	-
C <sub>3</sub> S (%)	62.35	-	-	-
C <sub>2</sub> S (%)	20.28	-	-	-
C <sub>3</sub> A (%)	1.42	-	-	-
C <sub>4</sub> AF (%)	5.83	-	-	-
Loss on ignition (%)	1.28	0.72	0.24	-
Specific gravity	3.15	2.90	2.64	1.80



**Fig. 3.** The dimensions of test specimens (unit: mm): (a) prism specimen; and (b) ring specimen.

steel ring. The steel ring had an outer diameter of 325 mm and a height of 152 mm. The outer diameter of the concrete ring was 457 mm. The thickness of concrete was 66 mm.

A total of sixteen specimens were prepared and tested, including twelve prisms (specimen group: Prism-1 to Prism-4) and four rings

**Table 3**Investigated cases for prism specimens and ring specimens.

Mixture design	Specimen group	Sensor deployment pattern	Adjacent helix spacing (mm)	Specimen amount
M1	Prism-1	Longitudinal	-	3
	Ring-1	Helix	25.4	1
M2	Prism-2	Longitudinal	-	3
	Ring-2	Helix	25.4	1
M3	Prism-3	Longitudinal	-	3
Ring-3	Helix	25.4	1	
M4	Prism-4	Longitudinal	-	3
	Ring-4	Helix	25.4	1

(specimen group: Ring-1 to Ring-4), as listed in Table 3. Prism-1 and Ring-1 were made using mixture M1; Prism-2 and Ring-2 were made using M2; Prism-3 and Ring-3 were made using M3; Prism-4 and Ring-4 were made using M4. For each mixture, three prism specimens and one ring specimen were tested, and a total of four ring specimens were prepared to evaluate the performance of the proposed method for evaluating the restrained shrinkage of UHPC. Three prisms were duplicated for each mixture design to characterize the extent of the uncertainties of UHPC, and the results measured from distributed fiber optic sensors in three specimens were validated by the results from a dial gauge, as recommended by ASTM C157 [54]. In addition, a crack scope was employed to measure the crack width for validating the crack measurement results from the distributed fiber optic sensors. The details of investigated cases are listed in Table 3.

## 3.3. Sensor installation and instrumentation

The prism and ring specimens were instrumented with fiber optic cables. Fiber optic cables were installed along the centerline of each prism specimen before concrete casting, as depicted in Figs. 4(a) and 4 (b). For each ring specimen, fiber optic cables were installed on the interior surface of the steel ring (Loop-1) and the exterior surface of the steel ring (Loop-2) before concrete casting. After the specimen was demolded, a fiber optic cable was installed on the exterior surface of the concrete (Loop-4), as shown in Fig. 4(c). The temperature sensor was utilized for temperature compensation. Another fiber optic cable (Loop-3) was installed to the middle of the concrete layer using painting tapes (thickness: 0.1 mm) and gauge fixing wires (diameter: 0.8 mm) before concrete casting. The tape was cut into stripes with a width of 5 mm and applied at regular intervals of 100 mm along the cable, and the fixing wires were used to fix the position of Loop-3 on mold. Fig. 4(d) shows

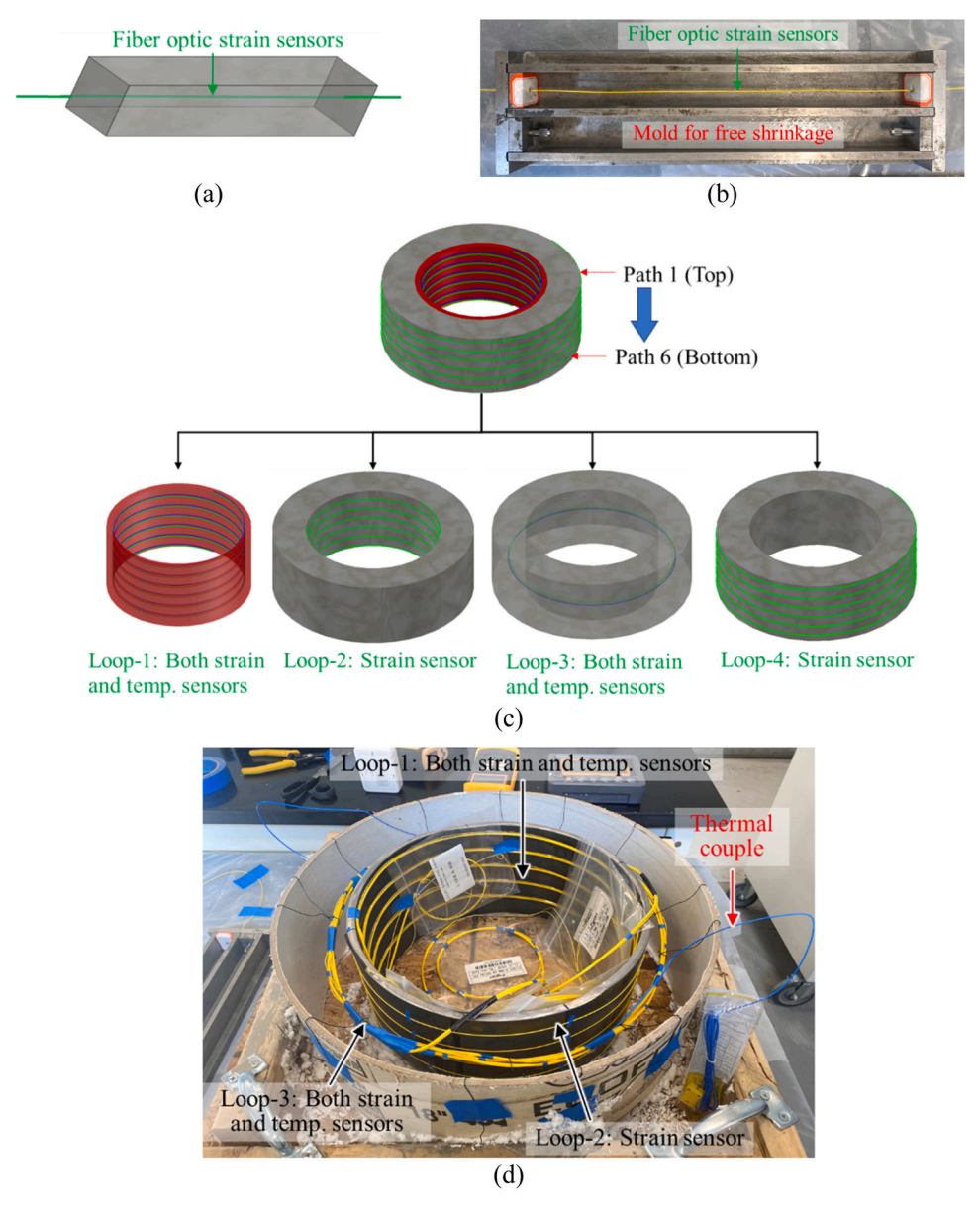


Fig. 4. Sensor installation: (a) layout of a fiber optic cable in a prism; (b) photo of a fiber optic cable in a prism; (c) layout of fiber optic cables in a ring; (d) photo of fiber optic cables in a ring.

the installation process of distributed sensors.

The sensor installation process includes four steps: (1) The outer surface of the concrete ring was thoroughly cleaned using sandpaper and wet wipes. (2) Tapes were cut into narrow stripes applied to discrete points along the designed path of the distributed sensor, spaced at 100 mm intervals, securing the fiber optic cable to the outer surface of the concrete. (3) A fast-setting adhesive was applied at the middle points of adjacent tapes to install the fiber optic cable. Once the adhesive cured (typically 20–30 seconds), the tapes were removed. (4) A two-part epoxy was used to firmly attach the distributed sensors to the concrete.

# 3.4. Casting and curing procedures

The mixtures were mixed using a mortar mixer (model: Hobart® HL-200), following the mixing procedure of UHPC developed in previous research [55]. Mini-slump tests were conducted for all batches before casting the prism and ring specimens for quality control. The specimens were cast on a vibrating table. The casting process is shown in Fig. 5.

After casting, all specimens were covered with a wet burlap and a

plastic sheet to prevent moisture loss, according to the curing requirement of AASHTO T334 [48]. The specimens were demolded after 24 hours of curing in the mold. Immediately after demolding, the specimens were stored in a room with controlled temperature (24  $\pm$  2 °C) and relatively humidity (50%  $\pm$  2%). The prisms were sealed using aluminum foil tape after demolded, as deposited in Fig. 5(a).

Further treatment was made for the ring specimens. The top surfaces and bottom surfaces of the ring specimens were sealed with wax to prevent moisture exchange, and only the exterior round surface was exposed to air, as shown in Fig. 5(d). For each of the ring specimens, fiber optic cables were attached to the exterior surface in the designed layout after the specimen was demolded, as shown in Fig. 5(e). The fiber optic cables survived in the installation, concrete casting, demolding, and curing, indicating that the fiber optic cables are rugged enough for practical applications without having to employ a special method for the construction.

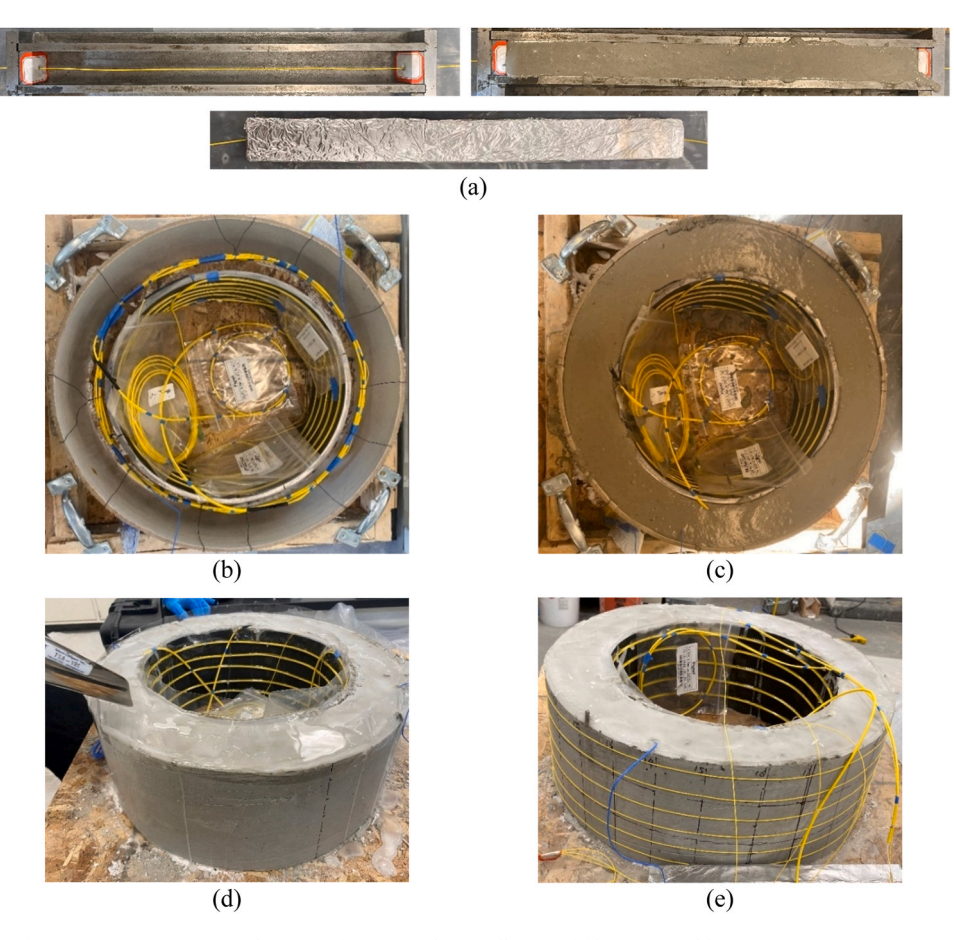


Fig. 5. Casting and curing of specimens: (a) casting and curing of a prism; (b) installation of fiber optic cables Loop-1 to Loop-3 on a ring specimen; (c) concrete casting of a ring specimen; (d) demolding and wax-sealing on the top surface of a ring specimen; and (e) installation of fiber optic cables Loop-4 on a ring specimen.

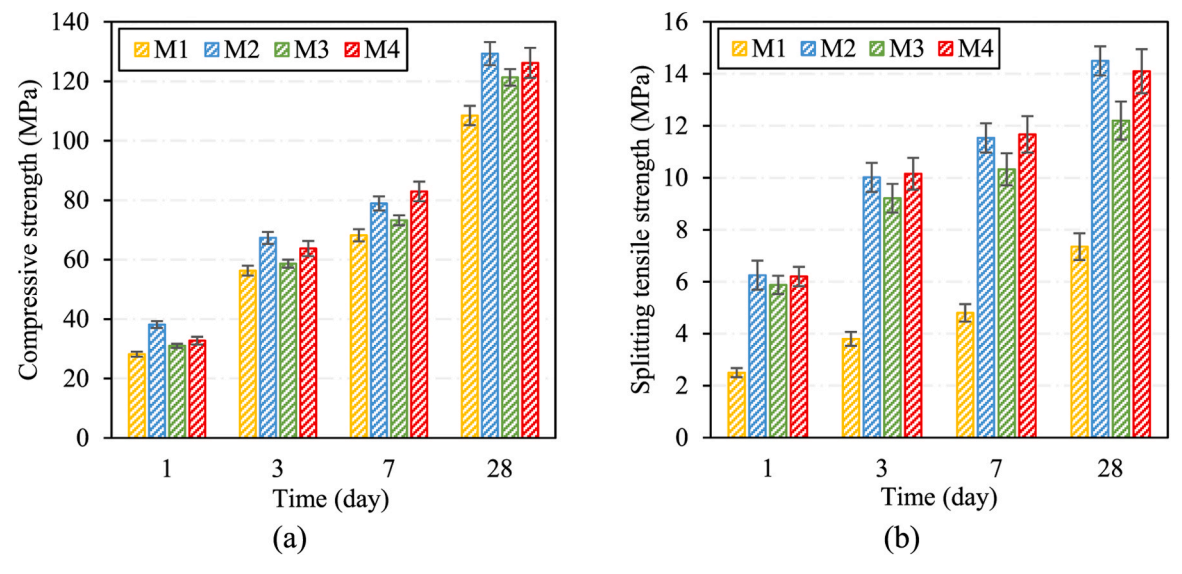


Fig. 6. Mechanical testing results: (a) compressive strength; and (b) splitting tensile strength.

# 3.5. Test set-up and protocol

The distributed fiber optic sensors deployed in different specimens were connected to form a continue sensor which was connected to the data acquisition system and the computer for data collection. A fiber optic cable free of strain change was utilized for temperature compensation. Continuous strains were measured from the distributed fiber

optic sensors on an hour basis which was deemed appropriate for shrinkage measurements. Visual inspection of cracks in the ring specimens was conducted using a digital crack scope (model: Dino-Lite Digital Microscope AM 4113ZTL; precision: 5  $\mu m)$  at 1 day, 3 days, 7 days, and 28 days. Once a crack was found, the crack scope was employed to capture the images of cracks, and the images were subsequently utilized to quantify the crack width.

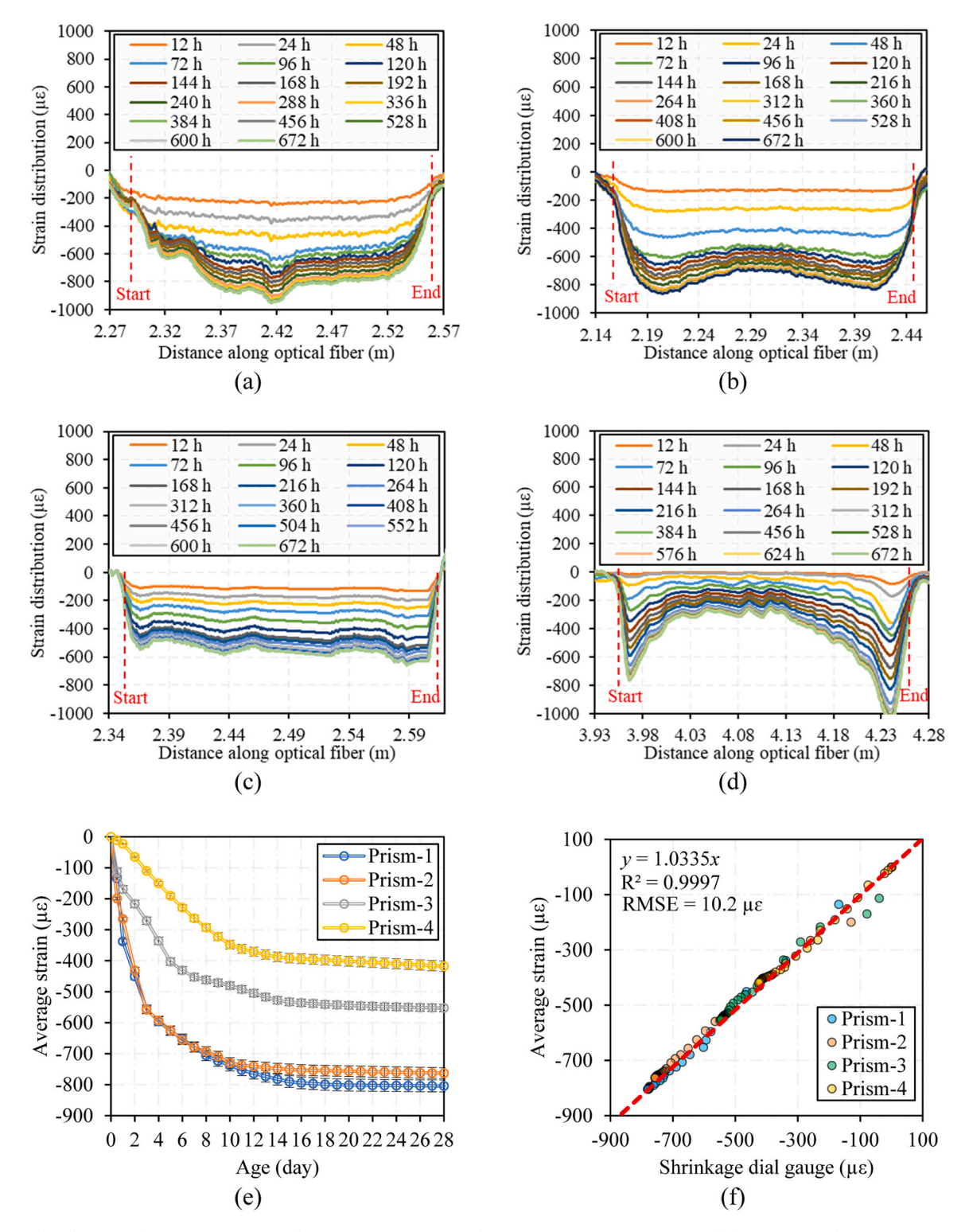


Fig. 7. Strain distributions of prisms: (a) Prism-1; (b) Prism-2; (c) Prism-3; (d) Prism-4; (e) average strains; and (f) comparison between average strains from distributed sensors and dial gauges.

# 4. Experimental results

# 4.1. Mechanical testing results

The compressive and tensile properties of the mixtures were evaluated according to ASTM C39 [56] and ASTM C496 [57], respectively. Three specimens were replicated for each test. The results of the compressive and splitting tensile strengths up to 28 days are shown in

Fig. 6(a) and Fig. 6(b), respectively. The 28 days compressive strength of three developed UHPC mixtures (M2, M3, and M4) are all greater than 120 MPa, which meet the meet the definition of UHPC, according to Portland Cement Association [58] and other researchers [59–61].

# 4.2. Autogenous shrinkage

Fig. 7 shows the strain distributions measured from the distributed

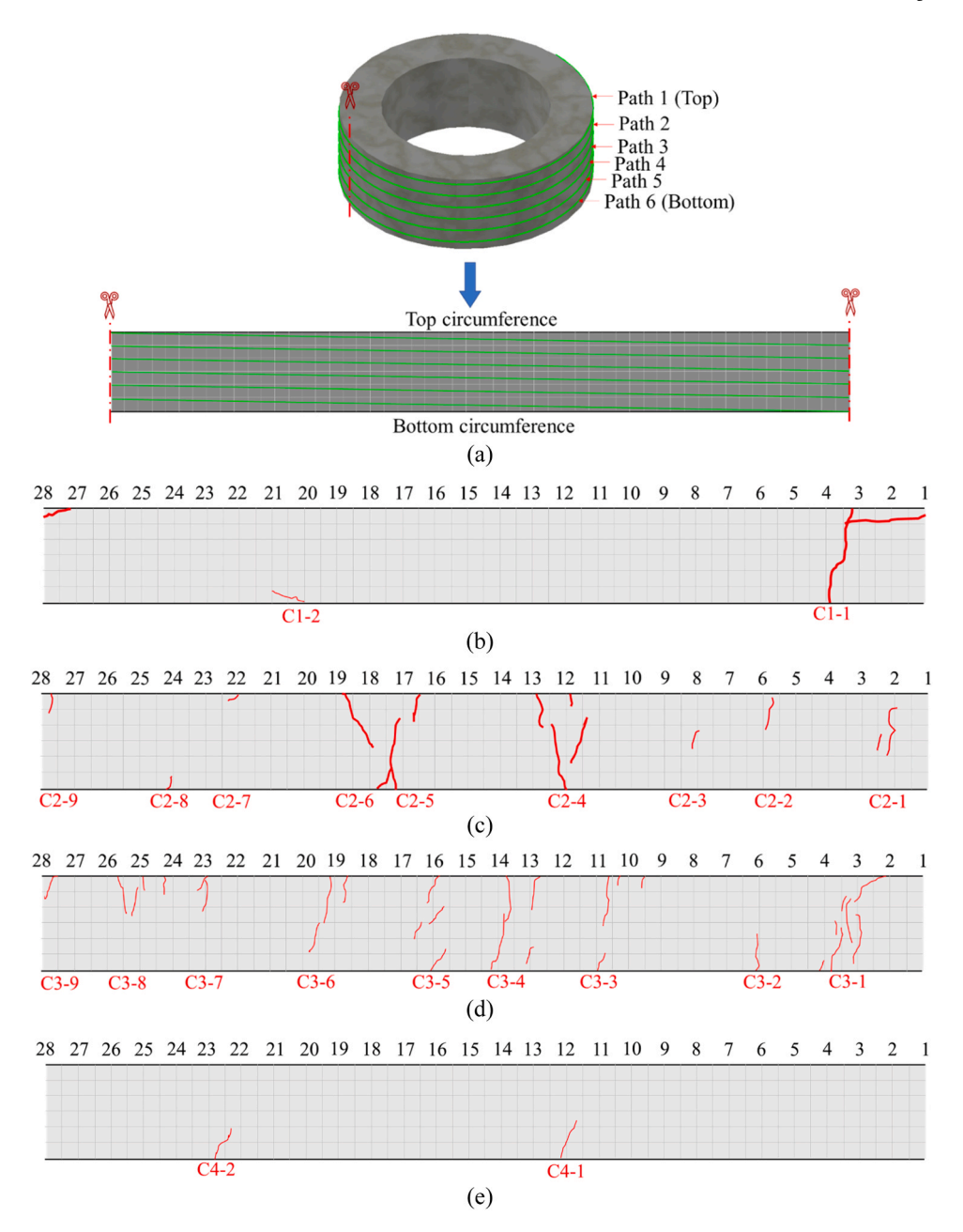


Fig. 8. Visual inspection of crack patterns for UHPC rings on the 28 days after demolding: (a) illustration of coordinate correlation; (b) Ring-1; (c) Ring-2; (d) Ring-3; and (e) Ring-4.

sensors in the prisms. The horizontal axis shows the strain distributions measured from the length of fiber optic cable installed on the prism specimen (from "Start" to "End" in Fig. 7), with the zero distance at the connector of the data acquisition system. The vertical axis is the strains measured from the fiber optic cable. For each group (Prism-1 to Prism-4), representative results from one specimen are displayed to show the patterns of strain distributions. Consistent results were obtained from other specimens. The fiber optic cable was subjected to the macro bending and strain transfer effects [27,36], which caused nonzero strains in the vicinity of the two ends of the fiber optic cable embedded in concrete.

Shrinkage caused nonuniform negative (compressive) strains along the length of distributed sensors. The strain magnitude increased over time, consistent with the development of shrinkage. In Prism-4, the magnitudes of strains at the center were much smaller than those at the two ends, as shown in Fig. 7(d). There are multiple possible reasons: (1) The two ends of the prisms were not fully sealed and have moisture loss,

which increased shrinkage due to the drying effect. (2) The two ends of the fiber optic cables were subjected to friction, which increased the compressive strains. (3) The unavoidable inhomogeneities of UHPC mixture along the length of the prism. In addition, the different shrinkage strains were exacerbated by the use of shrinkage reducing agent in mixture design M4 because the use of shrinkage reducing agent reduced the shrinkage strain, thereby making the difference between the strains at the two ends and the strains in the middle of the specimen more obvious. The preparation of all prisms was in accordance with ASTM C157 [54] and did not show an obvious low quality of the specimens. The presence of nonuniform shrinkage indicates that the existing method of measuring shrinkage introduces uncertainties and errors in the results. It is difficult to evaluate the quality of results in practice. Further research is necessary to fully understand the non-uniform strain distributions.

The average strains of each specimen's strain distribution in Prism-1 to Prism-4 group at different curing ages were calculated, as shown in

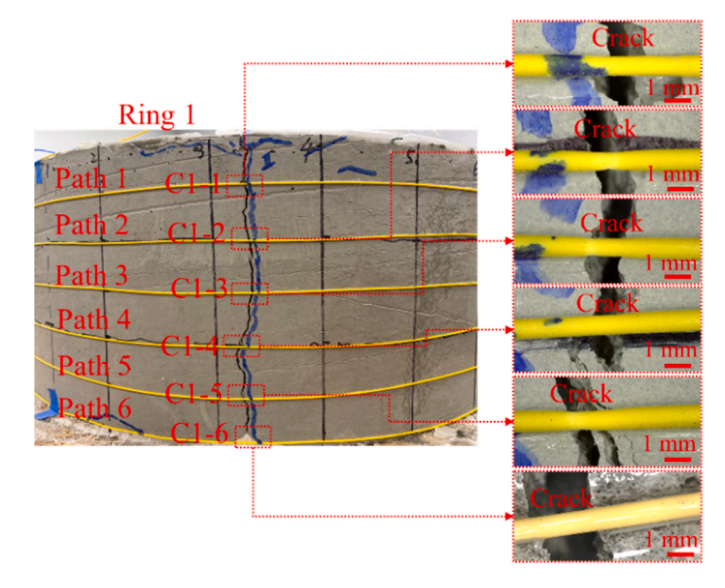


Fig. 9. Photo of the cracks and distributed sensor on the surface of specimen Ring-1 at 28 days.

Fig. 7(e). The results indicate that shrinkage strains increased rapidly at the beginning and then stabilized after 7 days. The average strains for each group were then compared with the strains measured by shrinkage dial gauges, as shown in Fig. 7(f). A straight line is employed to fit the data through linear regression. The coefficient of determination ( $R^2$ ) is calculated to be 0.9997 and the Root Mean Squared Error (RMSE) is calculated to be 10.2  $\mu\epsilon$ , which indicates a good consistency between the results obtained from the distributed sensors and the shrinkage dial gauges.

# 4.3. Restrained shrinkage

## 4.3.1. Visual observations

The cracking processes of four rings are shown in Fig. 8. The cracks on the external surface of the rings were inspected using a high-resolution camera and sensed by a distributed sensor loop-4 in each ring specimen. The cracks are marked by red lines. The cracks were designated as "Ci-j," where "C" means cracks, "i" is the number of a ring, and "j" is the number of a crack. The cracks were sequentially numbered from zone "1" to zone "28" along the horizontal direction.

Fig. 8(b) shows the crack pattern on the external surface of Ring-1. Two cracks were observed. The first crack C1-1 was a major crack, which initiated near zone "3" and zone "4" after the ring was demolded for 2 hours. C1-1 initiated at the bottom and the top, and propagated toward the middle of the ring. C1-1 penetrated the thickness of the concrete within 2 hours. When the time approached 672 hours (28 days), the second crack C1-2 occurred near the bottom of zone "20" and

zone "21". The intersection points of crack C1–1 and distributed sensor were captured by the crack scope, as shown in Fig. 9. The crack widths were measured using the crack scope.

Figs. 8(c) to 8(e) show the crack patterns of Ring-2 to Ring-4, respectively. With the use of steel fibers, micro-cracks were densely distributed on the surface of concrete, rather than major cracks in Ring-1. In Ring-2, nine micro-cracks were observed, and the first two cracks (C2-4 and C2-5) initiated at the bottom after the ring was demolded for 24 hours. With the increase of time, C2-4 and C2-5 propagated toward the top, and more cracks were generated. In Ring-3, nine micro-cracks were observed too. However, only one crack was generated at the bottom after the ring was demolded for 24 hours, and the other cracks were generated later than those of Ring-2. The number of cracks in Ring-3 is more than the number of cracks in Ring-2, as shown in Fig. 8. At the same age, Ring-3 showed narrower cracks than Ring-2, as shown in Fig. 15(b) and (c). In other words, Ring-3 showed more micro cracks than Ring-2. This can be attributed to the lower early-age tensile strength of mixture M3, which was used in Ring-3, as shown in Fig. 6(b). The use of lightweight aggregates for internal curing reduced both shrinkage and tensile strength of mixture M3. In Ring-4, no crack was found by bare eyes, and two micro-cracks were found by using the crack scope.

### 4.3.2. Strain distributions

The interaction between steel and concrete is illustrated in Fig. 10. Due to hydraulic reactions and moisture loss of concrete, shrinkage will be developed in the concrete ring. Since the shrinkage of concrete is restrained by the steel ring, the concrete will apply compressive stresses to the steel rings. As the reaction, the steel ring will apply radial forces to the concrete ring, generating tensile stresses along the circumference of the ring. When the tensile stresses are greater than the crack stress of the concrete, cracks will be generated in the concrete ring. Besides, a significant moisture gradient develops within the concrete under this drying condition, leading to non-uniform shrinkage along the radius of the concrete ring due to non-linear moisture diffusion [62]. Therefore, the self-restraint (ranging from no restraint on the outer surface to full restraint on the inner surface) introduces an additional force that contributes to concrete cracking [63]. Due to the combined effect, the maximum tensile stress takes place at the outer circumference of restrained concrete rings [64], and consequently, shrinkage cracks initiate from the outer surface and propagate toward the inner surfaces of concrete. The degree of self-restraint will be reduced with the propagation of cracks. The investigation for defining and quantifying the restrained degree for ring specimens is elaborated in Section 4.3.3.

The circumferential strains in concrete and steel rings were measured by distributed sensors. The strain distributions measured from the distributed sensors deployed on the exterior surfaces of the concrete rings are plotted in Fig. 11. As the shrinkage increased with time, cracks were generated in concrete. Fig. 11(a) plots the strain distributions measured from the six paths of the distributed sensor in Ring-1 (Loop-4 in Fig. 4). The strain peaks indicate cracks. The locations of peaks

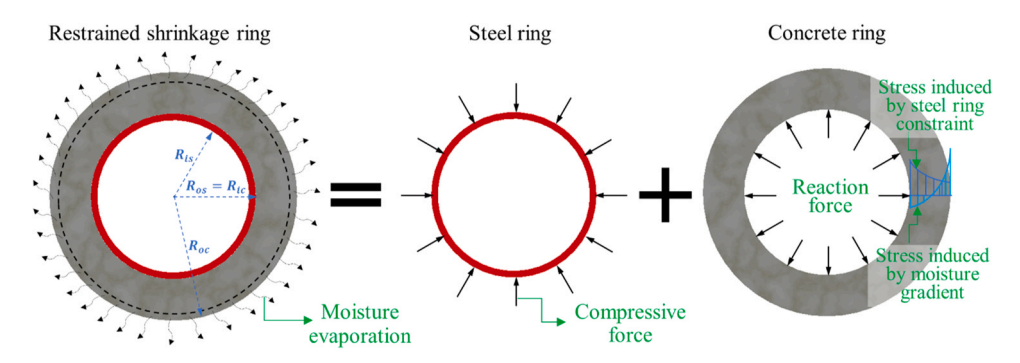


Fig. 10. Mechanism of cracking induced by the restrained shrinkage of concrete in rings.

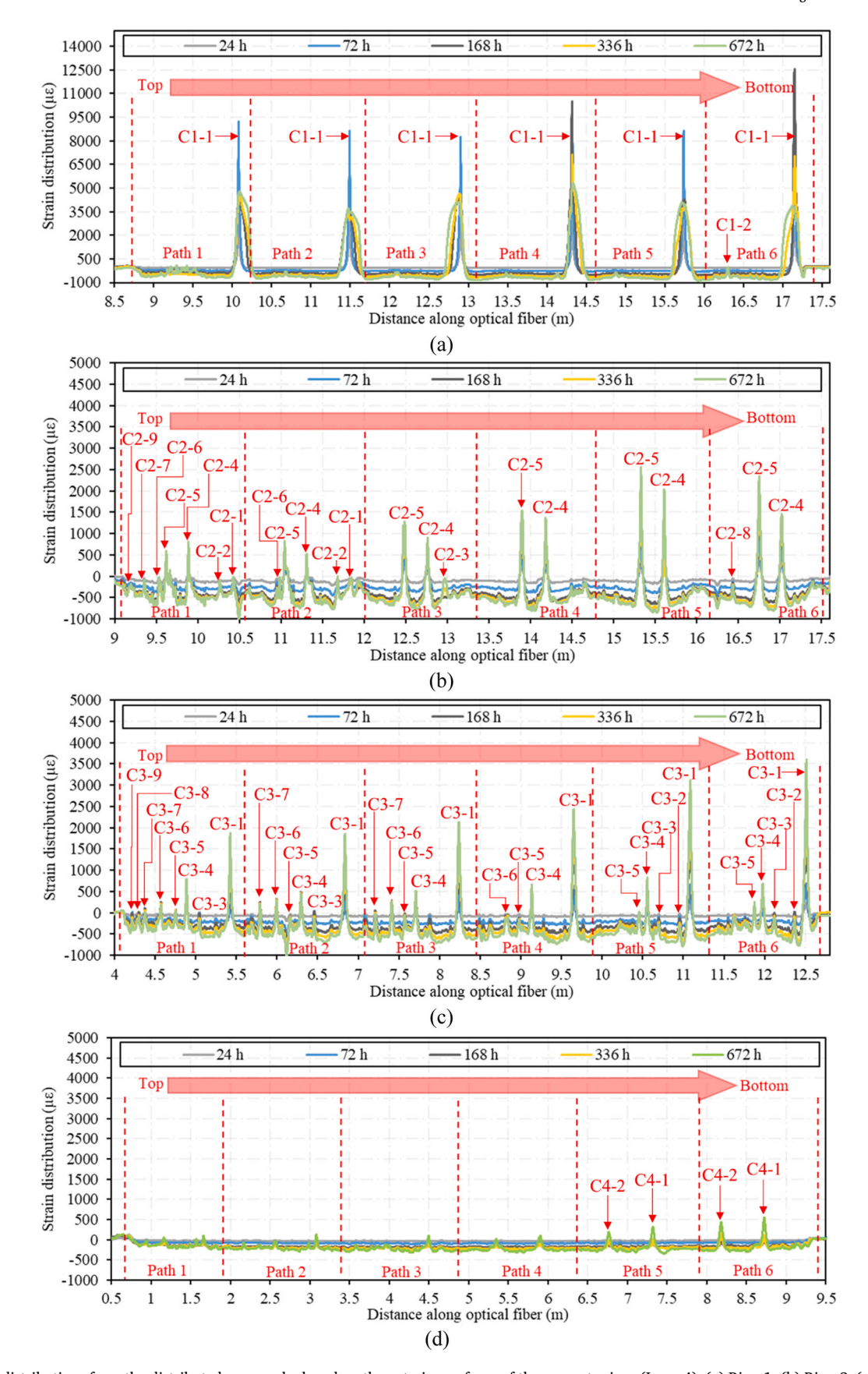


Fig. 11. Strain distributions from the distributed sensors deployed on the exterior surfaces of the concrete rings (Loop-4): (a) Ring-1; (b) Ring-2; (c) Ring-3; and (d) Ring-4.

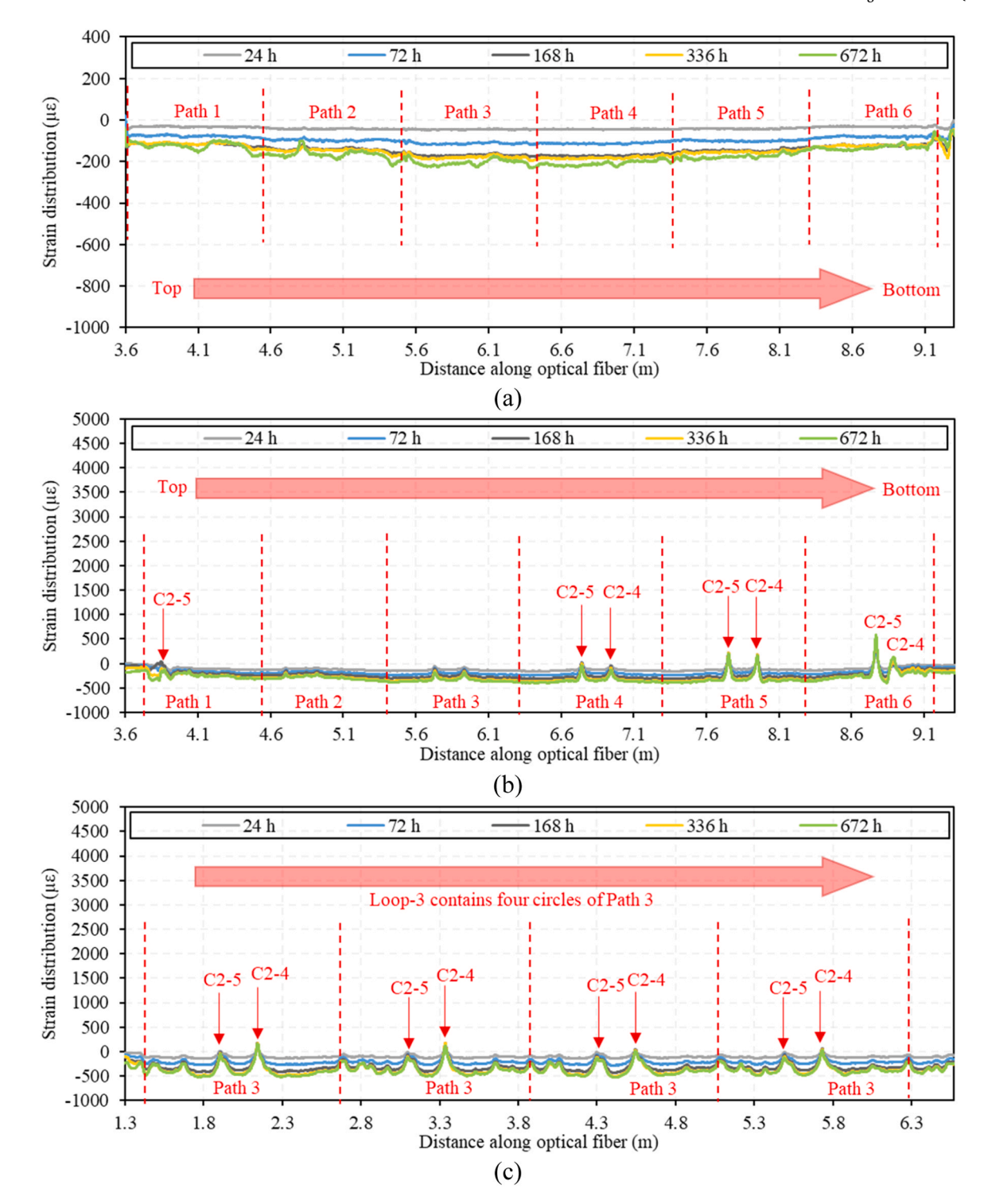


Fig. 12. Strain distributions from the rest distributed sensors deployed on Ring-2: (a) Loop-1; (b) Loop-2; and (c) Loop-3.

indicate the positions of cracks. The magnitudes of the peaks are associated with the crack width [35,44,65]. Overall, the magnitudes of the peaks near the top and bottom surfaces of Ring-1 are larger than those in the middle, consistent with the visual inspection of cracks. It was found that C1–1 initiated at the bottom and top and then propagated toward the middle of the ring. The highest peak was in Path 6 near the bottom surface of Ring-1.

With the development of shrinkage, C1–1 was widened, and interfacial debonding occurred in the fiber optic cable at 120 hours (5 days). The presence of interfacial debonding was indicated by the strain peaks

in the strain distributions. Fig. 11(a) shows that the widths of strain peaks increase, and the strain peaks decrease after interfacial debonding. The widening of the strain peaks is caused by fiber-coating interfacial slippage, as elaborated in reference [65]. When a crack passes through the fiber optic cable, debonding will occur at the fiber-coating interface and average the sudden deformation at the crack over a debonding length, thereby reducing the peak strain in the fiber core and preventing rupture of the fiber core. More details are available in references [35,44,65].

The strain distributions measured from Ring-2 to Ring-4 are shown in

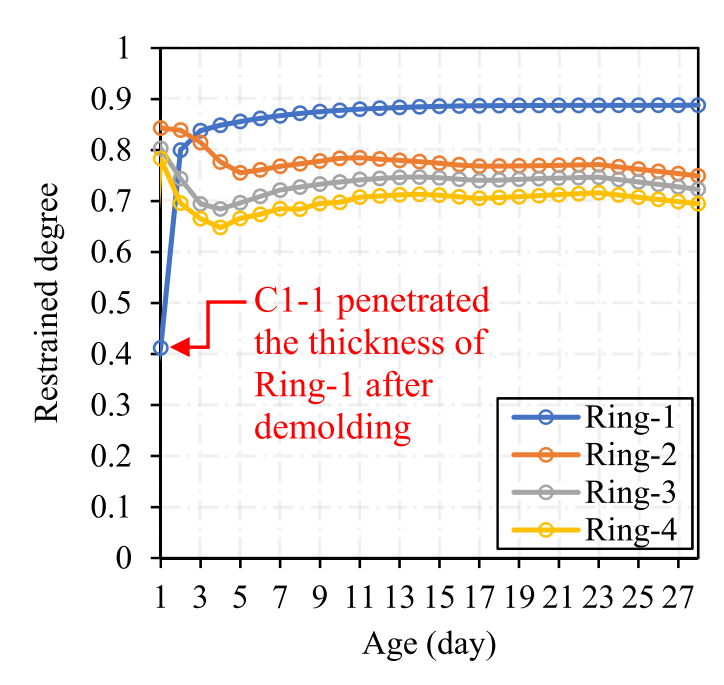


Fig. 13. Calculation results of restrained degree ( $\psi$ ) of different rings (Ring-1 to Ring-4).

Figs. 11(b) to 11(d), respectively. The locations of cracks identified from the strain distributions are consistent with visual inspection. As the concrete shrinkage increased over time, new peaks indicating new cracks emerged in the strain distributions, consistent with the visual observation of cracks in the Ring-2 to Ring-4 (Fig. 8). Another important finding is that the distributed sensor detected micro-cracks earlier than the digital crack scope. For example, C4–1 and C4–2 on Ring-4 were too narrow to be visually observed using the crack scope until 672 hours (28 days), but they were identified from the strain distributions measured from the distributed sensors much earlier.

The distributed sensors also showed the capacities of monitoring the crack penetration depth and concrete shrinkage at different thicknesses. Fig. 12 shows representative examples of strain distributions measured from distributed sensors deployed at different radii of Ring-2 (Loop-1 to Loop-3). Fig. 12(a) shows the strain distributions of distributed sensors attached on the inner surface of the steel ring (Loop-1). The strains in the middle of the steel ring (Path 2 to Path 5) are larger than the strains at the top or bottom of the steel ring (Path 1 and Path 6), consistent with the boundary conditions of the ring whose top and bottom surfaces were wax-sealed to prevent moisture exchange between the concrete and the ambient environment.

The strain peaks measured from Loop-2 and Loop-3 show that C2–4 and C2–5 penetrated through the thickness of concrete, as shown in Fig. 12(b) and Fig. 12(c). Another observation is that the restrained shrinkage increased with the radius of concrete. For instance, the shrinkage strains measured from Loop-2 (radius: 325 mm) are smaller than the shrinkage strains measured from Loop-3 (radius: 391 mm), and the shrinkage strains measured from Loop-4 (radius: 457 mm) are the largest, overall. Such a trend is consistent with the moisture loss condition at the different depths of concrete.

# 4.3.3. Restrained degree

In the case of restrained ring test, the restrained degree ( $\psi$ ) can be defined as follows [66,67]:

$$\Psi = \frac{U_{sh}(t) - U_{st}(t)}{U_{sh}(t)} = 1 - \frac{U_{st}(t)}{U_{sh}(t)}$$
(2)

where  $U_{sh}(t)$  is the free shrinkage deformation of the concrete ring;  $U_{st}(t)$  is the actual deformation of steel ring outer contact surface, which

is also the actual deformation of the concrete ring under the restraint. The restrained degree ( $\psi$ ) in Eq. (2) is defined at the concrete-steel interface ( $R_{os}=R_{ic}$ , Fig. 10) where the restraint is maximum. The value of  $\psi$  varies between 0 corresponding to no restraint ( $U_{st}(t)=U_{sh}(t)$ ) to 1 corresponding to total restraint ( $U_{st}(t)=0$ ).

Without considering moisture gradient, the free shrinkage deformation  $(U_{sh}(t))$  can be calculated based on the free shrinkage strain of concrete  $(\varepsilon_{sh}(t))$ :

$$U_{sh}(t) = \varepsilon_{sh}(t) \bullet R_{ic} \tag{3}$$

where  $R_{ic}$  is the inner radius of concrete ring.

The actual deformation of the restrained concrete under the restraint  $(U_{st}(t))$  can be calculated using the strain that is measured on the inner surface of the steel ring  $(\varepsilon_{st}(t))$  using Loop-1:

$$U_{st}(t) = \frac{1}{2} \frac{\epsilon_{st}(t)}{R_{os}^{2} + R_{is}^{2} - \mu_{s}(R_{os}^{2} - R_{is}^{2})}$$
 (4)

where  $\mu_s$  is the Poisson's ratio of steel;  $R_{is}$  and  $R_{os}$  are the inner radius and outer radius of steel ring, respectively.

Substituting Eqs. (3) and (4) into (2), the restrained degree ( $\psi$ ) can be written as follows:

$$\Psi = 1 - \frac{1}{2} \frac{\varepsilon_{st}(t)}{\varepsilon_{sh}(t)} \left[ \frac{R_{is}^2}{R_{os}^2} (1 + \mu_s) + (1 - \mu_s) \right]$$
 (5)

Fig. 13 shows the computed restrained degree ( $\psi$ ) of different ring specimens (Ring-1 to Ring-4). Overall, it can be observed that the restrained degree ( $\psi$ ) of Ring-2 to Ring-4 was in decrease trend as time passed due to the increase of shrinkage strain of UHPC. With involving steel fibers, lightweight sand, and shrinkage reduce agent, Ring-4 provides the lowest values of restrained degree compared with Ring-2 and Ring-3 at the same age. For Ring-1 without involving steel fiber, crack C1–1 penetrated the thickness of Ring-1 just 2 hours after demolding, so the value of  $\psi$  drops significantly at day 1 due to the release of constraint stress. However, the highest restrained degree ( $\psi$ ) was also found in Ring-1 to be 0.89 at 28 days.

# 4.4. Visualization of crack and restrained shrinkage

The strain distributions can be converted into images to make it more convenient for engineers to interpret the strain distributions for crack monitoring. The images are crack maps created by performing coordinate correlation, as shown in Fig. 8(a). The round surface of the concrete ring is converted into a plane surface. By correlating the coordinates, the strain distributions obtained from the distributed sensors in the concrete ring can be accurately mapped onto the plane surface. The coordinates of the fiber optic cable are described in a polar coordinate system and transformed into a Cartesian coordinate system. The circumference of the concrete ring becomes the length of the plane, and the height of the ring remains the height of the ring. The different paths of distributed fiber optic sensors (black dash line in Fig. 14) reveal the variation of strains and cracks over the height and circumference of the concrete rings.

Although the distributed fiber optic sensor is long, it cannot cover the entire exterior surface of the concrete because the adjacent paths of fiber optic cables have a spacing. In this study, the missing data between adjacent paths of fiber optic cables were obtained through biharmonic spline interpolant by using the surface fitting function of MATLAB. Then, the full strain distributions are plotted to show strain contours (Fig. 14), which can be used to visualize restrained shrinkage strain and induced cracks. In Fig. 14, the legend shows the magnitude of strains (unit:  $\mu\epsilon$ ), and the red color indicates cracks, and the deep blue color indicates large shrinkage. The locations of the cracks identified from the strain distributions were in good agreement with the visual inspection results. In Fig. 14(a), the widths of red areas are much wider than the widths of cracks, because the widths of red areas reflect the widths of

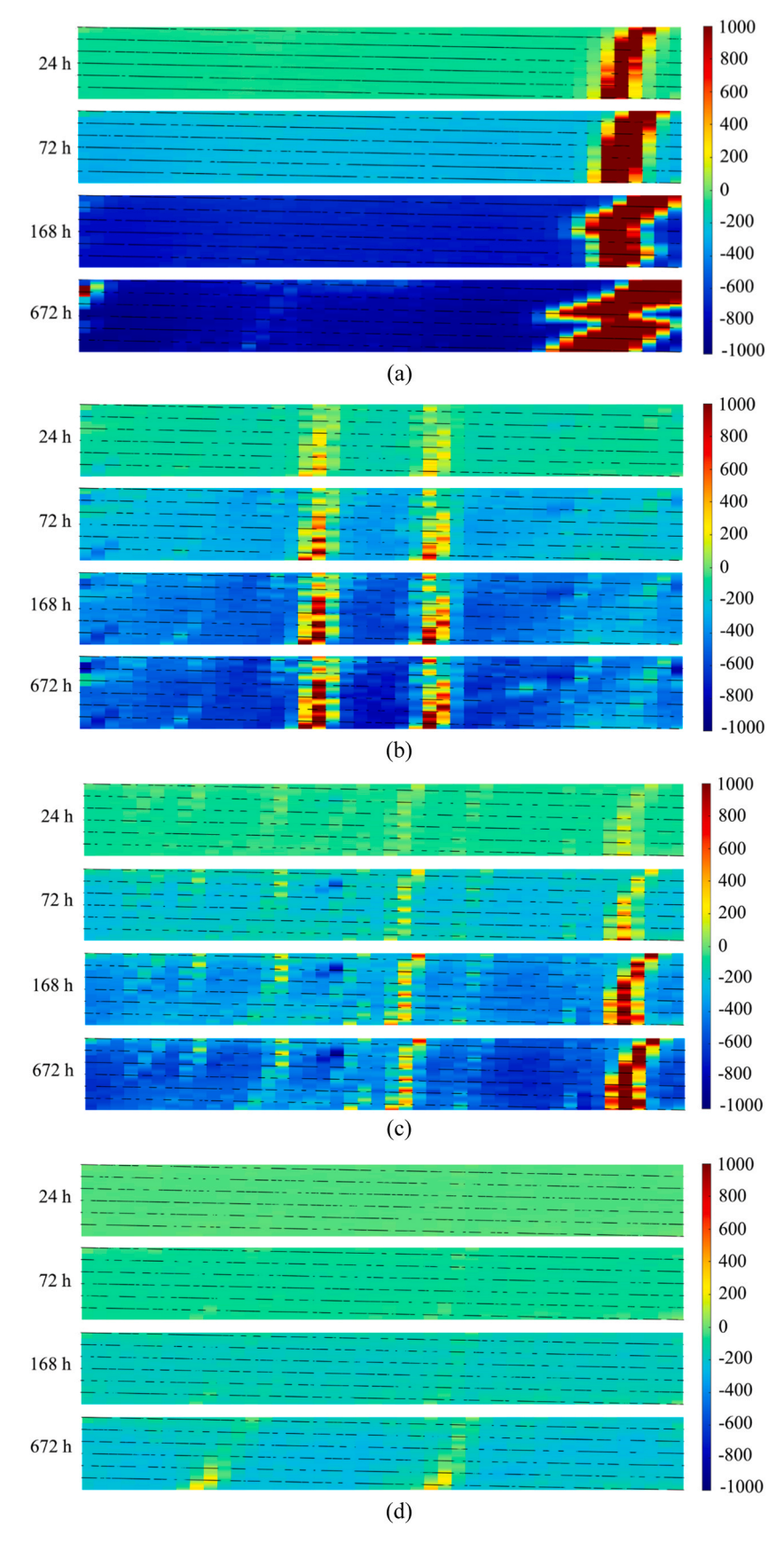
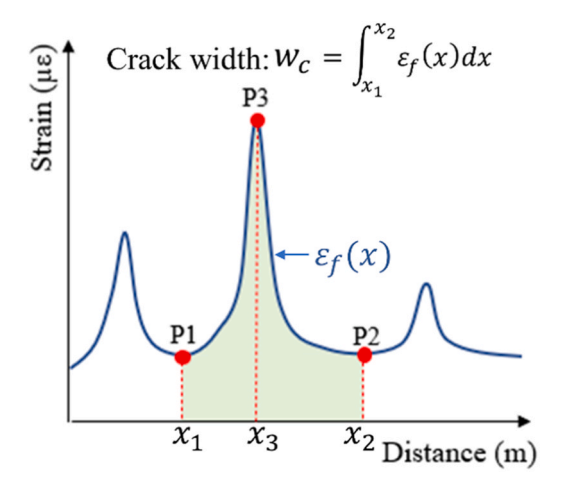


Fig. 14. Contours of the strain distributions measured from the Loop-4 distributed sensors (Unit: με): (a) Ring-1; (b) Ring-2; (c) Ring-3; and (d) Ring-4.



**Fig. 15.** Quantification of the crack width by performing integration of strain distribution [44].

strain peaks, rather than the widths of cracks. The widths of strain peaks are wide due to the presence of interfacial debonding, as elaborated in reference [35,65]. The crack maps are mainly used to visualize locations

of cracks.

### 4.5. Quantification of crack width

The crack width refers to the disparity in length changes between the fiber optic cable and the concrete at a specific crack. Recent studies have proven that the crack width is related to the fiber-coating interface slippage at crack intrinsically, and the interface slippage can be theoretically derived by the integration of the strain distribution in vicinity of the crack, as elaborated in reference [65]. In the vicinity of a crack, the strains in concrete are negligible, compared with the strain in the optical fiber due to cracks. Therefore, the integration of strain distributions measured in the vicinity of a crack reflects the crack width. When there are multiple cracks, the integration range of each crack is determined by the slope of the strain distribution. In other words, the points with zero slope were selected as  $x_1$  and  $x_2$  for evaluating the crack width.

In Fig. 15, point P3 refers to the peak strain, and the strain integration from  $x_1$  and  $x_2$  corresponds to points P1 and P2. More details about the calculation method are elaborated in references [35,44,65].

The results of crack widths calculated using the strain integration method and measured from the digital crack scope are compared in Fig. 15. The results obtained from the distributed sensors embedded

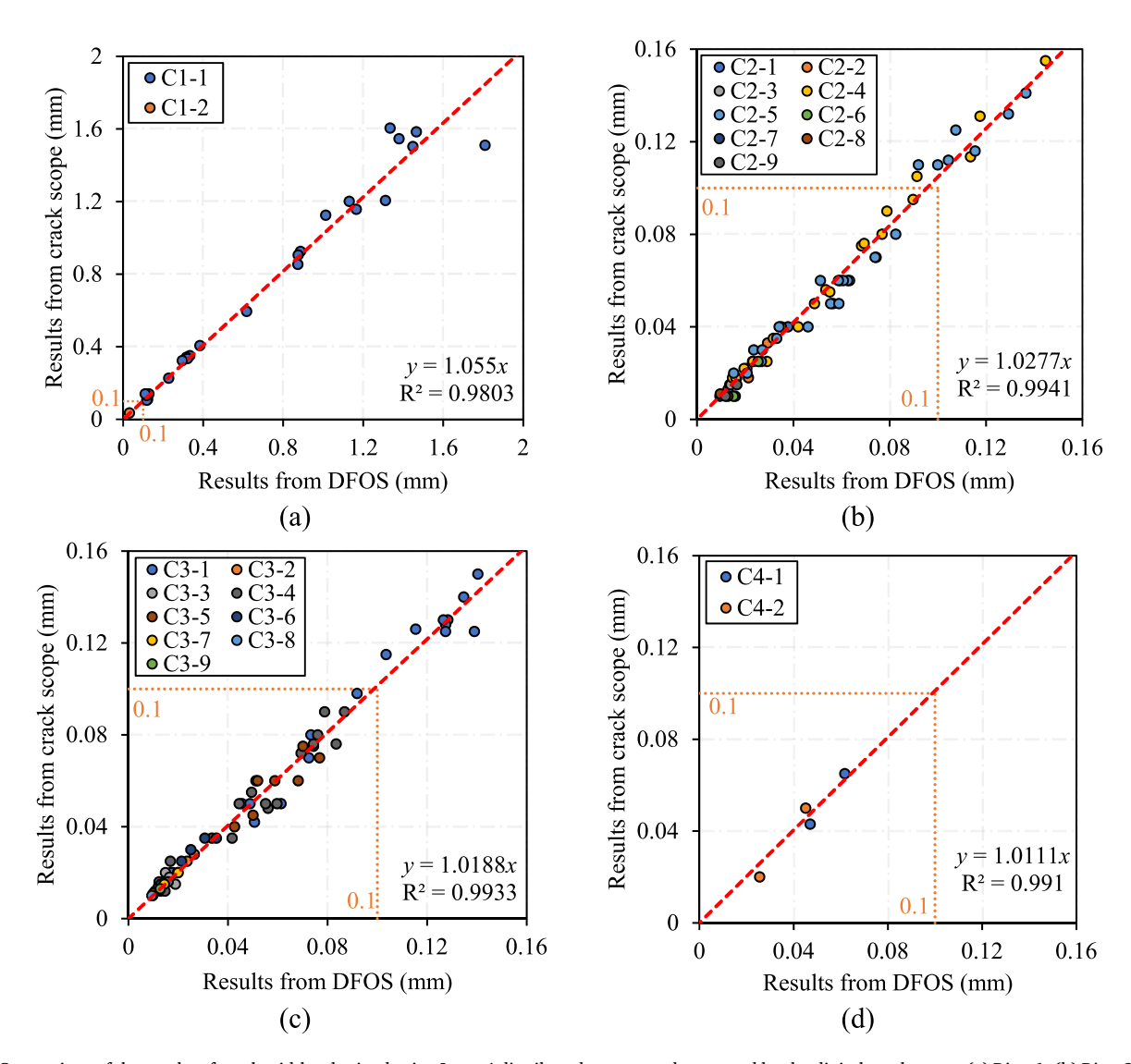


Fig. 16. Comparison of the results of crack widths obtained using Loop-4 distributed sensors and measured by the digital crack scope: (a) Ring-1; (b) Ring-2; (c) Ring-3; and (d) Ring-4. (Note: "DFOS" refers to distributed fiber optic sensor).

inside the concrete (Loop-2 and Loop-3) are not included in Fig. 16, as the crack scope is unable to inspect hidden cracks. A straight line has been utilized to fit the data points using linear regression. According to existing studies [68,69], when the crack width of concrete is lower than 100  $\mu m$ , the crack does not largely affect the permeability and often can be healed automatically through secondary hydraulic reactions. Therefore, 100  $\mu m$  (or 0.1 mm) was usually selected as the criterion for evaluating the durability of UHPC.

The crack width results of Ring-1 are shown in Fig. 16(a). The coefficient of determination ( $R^2$ ) is 0.9803, indicating a robust correlation between the crack width measurements obtained from the distributed sensors and those obtained from the crack scope. The slope of the fitting line (1.055) is used to correct the results from the distributed sensors. The widths of C1–1 were much larger than 100  $\mu m$  from the beginning of the testing, indicating that Ring 1 had poor durability.

The results of Ring-2 are shown in Fig. 16(b). The  $R^2$  is 0.9941, which also shows a strong correlation between the crack width measurements obtained from the distributed sensors and those obtained from the crack scope. The slope of the fitting line is 1.0277. Except for cracks C2–4 and C2–5 that were wider than 100  $\mu m$  at 168 hours (7 days), most cracks were narrower than 100  $\mu m$ . The results indicated that Ring-2 had better durability due to the use of steel fibers.

The results of Ring-3 are shown in Fig. 16(c). The  $R^2$  is 0.9933. The slope of the fitting line is 1.0188. Except for crack C3–1, which was wider than 100  $\mu m$  at 168 hours (7 days), the other cracks were narrower than 100  $\mu m$ . Overall, the number and widths of cracks in Ring-3 are smaller than those of Ring-2, because the use of lightweight sand reduced the shrinkage of concrete due to the internal curing effect [60, 70]

The results of Ring-4 are shown in Fig. 16(d). The  $R^2$  is 0.9910. The slope of the fitting line is 1.0111. All the cracks were narrower than 100  $\mu m$ , indicating that the combined use of steel fibers, internal curing agent (lightweight sand), and shrinkage reducing agent is effective in minimizing shrinkage and cracking of UHPC. The development of low-shrinkage UHPC helps extend the service life and enhance durability of concrete structures.

The errors of crack width can be attributed to multiple reasons: (1) Variation in measurement positions: The crack scope and the distributed sensor were positioned differently. The presence of the fiber optic cable caused a slight shift in the crack width measurement positions compared to the fiber optic cable. (2) Measurement errors from strain distributions: The strain distributions measured from the distributed sensor may contain inherent errors which are accumulated during the integration of strains in the calculation of crack width. (3) Inclined angle between fiber optic cable and cracks: Errors arise from the inclined angle between fiber optic cables and cracks, which are further increased due to combined opening-sliding kinetics at the cracks. (4) Uncertainty of UHPC: Those analytical values and discussion of the materials' properties may have uncertainty since they were obtained from only one test.

## 5. Conclusions

This paper presents a method to directly measure shrinkage and cracks in UHPC subjected to restrained shrinkage using distributed fiber optic sensors with high resolution. Laboratory tests were conducted to evaluate the performance of the method and the effects of steel fibers, internal curing agent (lightweight sand), and shrinkage reducing agent on the shrinkage and cracks of UHPC. This research supports the development of low-shrinkage UHPC. Based on the above investigation, the following conclusions are drawn:

 Distributed fiber optic sensors can be applied to measure shrinkage strains and monitor the initiation and development of shrinkage cracks of restrained UHPC. The cracks were able to be located and quantified by analyzing the strain distributions obtained from distributed sensors. Crack maps can be created to visualize the

- distribution of cracks by converting the strain distributions into strain contour images.
- The methods for evaluating shrinkage using prism and ring specimens involve nonuniform shrinkage strains which are neglected when the average shrinkage strain of a specimen is used, thereby introducing uncertainties in the results of shrinkage. It is recommended to conduct further research to develop reliable and robust methods to evaluate shrinkage.
- Using steel fibers, lightweight sand, and shrinkage reducing agent is
  effective in reducing shrinkage and mitigating cracks. It is promising
  to eliminate restrained shrinkage cracks by combining the use of
  steel fibers, internal curing agent, and shrinkage reducing agent. In
  this research, the restrained shrinkage of UHPC decreased from 809
  με to 245 με; and the maximum crack width decreased from
  1.605 mm to 0.065 mm.

## CRediT authorship contribution statement

Xiao Tan: Writing – original draft, Visualization, Validation, Software, Methodology, Investigation, Formal analysis, Data curation, Conceptualization. Qinghua Zhang: Writing – review & editing. Jiang Du: Writing – review & editing, Methodology, Investigation, Data curation. Yi Bao: Writing – review & editing, Supervision, Project administration, Funding acquisition, Conceptualization. Weina Meng: Writing – review & editing, Supervision, Resources, Conceptualization.

## **Declaration of Competing Interest**

The authors declare the following financial interests/personal relationships which may be considered as potential competing interests: Yi Bao reports financial support was provided by the United States Department of Transportation and United States National Science Foundation. Weina Meng reports financial support was provided by the United States National Science Foundation.

## **Data Availability**

Data will be made available on request.

## Acknowledgement

This research was funded by the United States Department of Transportation [grant numbers 693JK31950008CAAP and 693JK32310008POTA] and the United States National Science Foundation [grant numbers CMMI 2046407 and CPS 2305882].

## References

- S. Ray, J.C. Kishen, Fatigue crack growth due to overloads in plain concrete using scaling laws, Sadhana 37 (1) (2012) 107–124, https://doi.org/10.1007/s12046-012.006.01
- [2] T.V. Do, T.M. Pham, H. Hao, Impact force profile and failure classification of reinforced concrete bridge columns against vehicle impact, Eng. Struct. 183 (2019) 443–458, https://doi.org/10.1016/j.engstruct.2019.01.040.
- [3] O. Pekau, Z. Chuhan, F. Lingmin, Seismic fracture analysis of concrete gravity dams, Earthq. Eng. Struct. Dyn. 20 (4) (1991) 335–354, https://doi.org/10.1002/ ege.4290200404.
- [4] M. Safiuddin, A. Kaish, C.-O. Woon, S.N. Raman, Early-age cracking in concrete: causes, consequences, remedial measures, and recommendations, Appl. Sci. 8 (10) (2018) 1730, https://doi.org/10.3390/app8101730.
- [5] H. Beushausen, M. Alexander, Failure mechanisms and tensile relaxation of bonded concrete overlays subjected to differential shrinkage, Cem. Concr. Res. 36 (10) (2006) 1908–1914, https://doi.org/10.1016/j.cemconres.2006.05.027.
- [6] L. Fan, Y. Bao, Review of fiber optic sensors for corrosion monitoring in reinforced concrete, Cem. Concr. Compos. 120 (2021) 104029, https://doi.org/10.1016/j. cemconcomp.2021.104029.
- [7] E. Fehling, M. Schmidt, J. Walraven, T. Leutbecher, S. Fröhlich, Ultra-High Performance Concrete UHPC: Fundamentals, Design, Examples, John Wiley & Sons, 2014, https://doi.org/10.1002/9783433604076.

- [8] V.C. Li, Engineered Cementitious Composites (ECC): Bendable Concrete for Sustainable and Resilient Infrastructure, Springer, 2019, https://doi.org/10.1007/ 078 2 62 5942 5
- [9] W. Meng, K.H. Khayat, Effect of graphite nanoplatelets and carbon nanofibers on rheology, hydration, shrinkage, mechanical properties, and microstructure of UHPC, Cem. Concr. Res. 105 (2018) 64–71, https://doi.org/10.1016/j. cemconres.2018.01.001.
- [10] R. Henkensiefken, D. Bentz, T. Nantung, J. Weiss, Volume change and cracking in internally cured mixtures made with saturated lightweight aggregate under sealed and unsealed conditions, Cem. Concr. Compos. 31 (7) (2009) 427–437, https://doi. org/10.1016/j.cemconcomp.2009.04.003.
- [11] X. Tan, S. Mahjoubi, Q. Zhang, D. Dong, Y. Bao, A framework for improving bridge resilience and sustainability through optimizing high-performance fiber-reinforced cementitious composites, J. Infrastruct. Preserv. Resil. 3 (1) (2022) 1–18, https:// doi.org/10.1186/s43065-022-00067-0.
- [12] ACI 209R-92 (1992). "Prediction of creep, shrinkage, and temperature effects in concrete structures." American Concrete Institute, USA. http://civilwares.free.fr/ ACI/MCP04/209r 92.pdf. Accessed on June 1, 2023.
- [13] fib Bulletin No. 65, Ernst & Sohn, Wiley, 2013, https://doi.org/10.1002/
- [14] K. Sakata, T. Shimomura, Recent progress in research on and code evaluation of concrete creep and shrinkage in Japan, J. Adv. Concr. Technol. 2 (2) (2004) 133–140, https://doi.org/10.3151/jact.2.133.
- [15] D. Partov, V. Kantchev, Gardner&Lockman model (2000) and its application in numerical analysis of composite beams, Procedia Eng. 40 (2012) 357–362, https://doi.org/10.1016/j.proeng.2012.07.108.
- [16] Z.P. Bazant, S. Baweja, Creep and shrinkage prediction model for analysis and design of concrete structures: Model B3, Acids Spec. Publ. 194 (2000) 1–84, https://doi.org/10.14359/9889.
- [17] R. Wendner, M. Hubler, Z. Bažant, The B4 model for multi-decade creep and shrinkage prediction, Mech. Phys. Creep, Shrinkage, Durab. Concr.: A Tribut. ZdeňK. P. BažAnt. (2013) 429–436, https://doi.org/10.1061/ 9780784413111.051.
- [18] D.-Y. Yoo, H.-O. Shin, Y.-S. Yoon, Ultrasonic monitoring of setting and strength development of ultra-high-performance concrete, Materials 9 (4) (2016) 294, https://doi.org/10.3390/ma9040294.
- [19] T. Watanabe, C. Hashimoto, Evaluation of shrinkage and cracking in concrete of ring test by acoustic emission method, Mod. Phys. Lett. B 29 (06n07) (2015) 1540033, https://doi.org/10.1142/S0217984915400333.
- [20] W. Wang, M. Xu, Y. Bao, Assessment of fracture process of engineered cementitious composite (ECC) by time-frequency analysis of acoustic emission signals, Smart Mater. Struct. 32 (4) (2023) 044003, https://doi.org/10.1088/1361-665X/acc1ba.
- [21] Piérard, J., Pollet, V., & Cauberg, N. (2006). "Mitigating autogenous shrinkage in HPC by internal curing using superabsorbent polymers." In International RILEM conference on volume changes of hardening concrete: Testing and mitigation, Paris, France. pp. 97-106. https://www.rilem.net/images/publis/pro052-011.pdf. Accessed on June 1. 2023.
- [22] Y. Lecieux, E. Roziere, C. Lupi, D. Leduc, M.L. François, Towards a 3D shrinkage measurement in concrete using an embedded strain sensor, Smart Mater. Struct. 27 (10) (2018) 105032, https://doi.org/10.1088/1361-665X/aadbd5.
- [23] S. Bakoss, A. Burfitt, L. Cridland, Measurement of strains in concrete members with vibrating wire strain gauges, Aust. Road. Res. 7 (3) (1977) 20–26, https://trid.trb. org/view/1208840. Accessed on June 1, 2023.
- [24] Z. Yazdizadeh, H. Marzouk, M.A. Hadianfard, Monitoring of concrete shrinkage and creep using Fiber Bragg Grating sensors, Constr. Build. Mater. 137 (2017) 505–512, https://doi.org/10.1016/j.conbuildmat.2017.01.084.
- [25] Y. Bao, M.S. Hoehler, L.Y. Choe, M. Klegseth, G. Chen, "Monitoring early-age shrinkage strain and temperature distributions in full-scale steel-concrete composite beams with distributed fiber optic sensors." Proc., 11th International Workshop on, Struct. Heath Monit. (IWSHM) (2017), https://doi.org/10.12783/ shm2017/14023.
- [26] Y. Bao, M. Valipour, W. Meng, K.H. Khayat, G. Chen, Distributed fiber optic sensor-enhanced detection and prediction of shrinkage-induced delamination of ultra-high-performance concrete overlay, Smart Mater. Struct. 26 (8) (2017) 085009, https://doi.org/10.1088/1361-665X/aa71f4.
- [27] M. Yan, X. Tan, S. Mahjoubi, Y. Bao, Strain transfer effect on measurements with distributed fiber optic sensors, Autom. Constr. 139 (2022) 104262, https://doi. org/10.1016/j.autcon.2022.104262.
- [28] B. Shi, D. Zhang, H. Zhu, C. Zhang, K. Gu, H. Sang, H. Han, M. Sun, J. Liu, DFOS applications to geo-engineering monitoring, Photon. Sens. 11 (2021) 158–186, https://doi.org/10.1007/s13320-021-0620-y.
- [29] H. Wijaya, P. Rajeev, E. Gad, Distributed optical fibre sensor for infrastructure monitoring: field applications, Opt. Fiber Technol. 64 (2021) 102577, https://doi. org/10.1016/j.yofte.2021.102577.
- [30] M. Enckell, B. Glisic, F. Myrvoll, B. Bergstrand, Evaluation of a large-scale bridge strain, temperature and crack monitoring with distributed fibre optic sensors, J. Civ. Struct. Health Monit. 1 (2011) 37–46, https://doi.org/10.1007/s13349-011.0004.x
- [31] J. Gómez, J.R. Casas, S. Villalba, Structural health monitoring with distributed optical fiber sensors of tunnel lining affected by nearby construction activity, Autom. Constr. 117 (2020) 103261, https://doi.org/10.1016/j. autcon.2020.103261.
- [32] H. Li, H. Zhu, H. Wu, B. Zhu, B. Shi, Experimental investigation on pipe-soil interaction due to ground subsidence via high-resolution fiber optic sensing, Tunn. Undergr. Space Technol. 127 (2022) 104586, https://doi.org/10.1016/j. tust.2022.104586.

- [33] C. Du, S. Dutta, P. Kurup, T. Yu, X. Wang, A review of railway infrastructure monitoring using fiber optic sensors, Sens. Actuators A: Phys. 303 (2020) 111728, https://doi.org/10.1016/j.sna.2019.111728.
- [34] H. Zhou, Z. Pan, Z. Liang, C. Zhao, Y. Zhou, F. Wang, Temperature field reconstruction of concrete dams based on distributed optical fiber monitoring data, KSCE J. Civ. Eng. 23 (2019) 1911–1922, https://doi.org/10.1007/s12205-019-07974
- [35] X. Tan, Y. Bao, Measuring crack width using a distributed fiber optic sensor based on optical frequency domain reflectometry, Measurement 172 (2021) 108945, https://doi.org/10.1016/j.measurement.2020.108945.
- [36] X. Tan, Y. Bao, Q. Zhang, H. Nassif, G. Chen, Strain transfer effect in distributed fiber optic sensors under an arbitrary field, Autom. Constr. 124 (2021) 103597, https://doi.org/10.1016/j.autcon.2021.103597.
- [37] S. Mahjoubi, X. Tan, Y. Bao, Inverse analysis of strain distributions sensed by distributed fiber optic sensors subject to strain transfer, Mech. Syst. Signal Process. 166 (2022) 108474, https://doi.org/10.1016/j.ymssp.2021.108474.
- [38] X. Tan, P. Guo, X. Zou, Y. Bao, Buckling detection and shape reconstruction using strain distributions measured from a distributed fiber optic sensor, Measurement 200 (2022) 111625, https://doi.org/10.1016/j.measurement.2022.111625.
- [39] X. Tan, L. Fan, Y. Huang, Y. Bao, Detection, visualization, quantification, and warning of pipe corrosion using distributed fiber optic sensors, Autom. Constr. 132 (2021) 103953, https://doi.org/10.1016/j.autcon.2021.103953.
- [40] L. Fan, X. Tan, Q. Zhang, W. Meng, G. Chen, Y. Bao, Monitoring corrosion of steel bars in reinforced concrete based on helix strains measured from a distributed fiber optic sensor, Eng. Struct. 204 (2020) 110039, https://doi.org/10.1016/j. engstruct.2019.110039.
- [41] Y. Bao, G. Chen, Strain distribution and crack detection in thin unbonded concrete pavement overlays with fully distributed fiber optic sensors, 011008-011008, Opt. Eng. 55 (1) (2016), https://doi.org/10.1117/1.0E.55.1.011008.
- [42] Y. Bao, F. Tang, Y. Chen, W. Meng, Y. Huang, G. Chen, Concrete pavement monitoring with PPP-BOTDA distributed strain and crack sensors, Smart Struct. Syst. 18 (3) (2016) 405–423, https://doi.org/10.12989/sss.2016.18.3.405.
- [43] H. Bai, D. Guo, W. Wang, X. Tan, M. Yan, G. Chen, Y. Bao, Experimental investigation on flexural behavior of steel-concrete composite floor slabs with distributed fiber optic sensors, J. Build. Eng. 54 (2022) 104668, https://doi.org/ 10.1016/j.jobe.2022.104668.
- [44] X. Tan, A. Abu-Obeidah, Y. Bao, H. Nassif, W. Nasreddine, Measurement and visualization of strains and cracks in CFRP post-tensioned fiber reinforced concrete beams using distributed fiber optic sensors, Autom. Constr. 124 (2021) 103604, https://doi.org/10.1016/j.autcon.2021.103604.
- [45] Y. Bao, W. Meng, Y. Chen, G. Chen, K.H. Khayat, Measuring mortar shrinkage and cracking by pulse pre-pump Brillouin optical time domain analysis with a single optical fiber, Mater. Lett. 145 (2015) 344–346, https://doi.org/10.1016/j. matlet.2015.01.140.
- [46] J.S. Yager, N.A. Hoult, E.C. Bentz, J.E. Woods, Measurement of restrained and unrestrained shrinkage of reinforced concrete using distributed fibre optic sensors, Sensors 22 (23) (2022) 9397, https://doi.org/10.3390/s22239397.
- [47] M.F. Bado, J.R. Casas, A. Dey, C.G. Berrocal, G. Kaklauskas, I. Fernandez, R. Rempling, Characterization of concrete shrinkage induced strains in internally-restrained RC structures by distributed optical fiber sensing, Cem. Concr. Compos. 120 (2021) 104058, https://doi.org/10.1016/j.cemconcomp.2021.104058.
   [48] AASHTO T 334-08 (2020). "Standard method of test for estimating the cracking
- [48] AASHTO T 334-08 (2020). "Standard method of test for estimating the cracking tendency of concrete," American Association of State and Highway Transportation Officials, Washington, D.C., USA. https://standards.globalspec.com/std/2028853/ aashto-t-334. Accessed on June 1, 2023.
- [49] X. Tan, S. Poorghasem, Y. Huang, X. Feng, Y. Bao, Monitoring of pipelines subjected to interactive bending and dent using distributed fiber optic sensors, Autom. Constr. 160 (2024) 105306, https://doi.org/10.1016/j. autcon.2024.105306.
- [50] D.K. Gifford, S.T. Kreger, A.K. Sang, M.E. Froggatt, R.G. Duncan, M.S. Wolfe, B. J. Soller, "Swept-wavelength interferometric interrogation of fiber Rayleigh scatter for distributed sensing applications.". Proc., Fiber Optic Sensors and Applications V, International Society for Optics and Photonics, 2007, p. 67700F, https://doi.org/10.1117/12.734931.
- [51] S. Rizzolo, J. Périsse, A. Boukenter, Y. Ouerdane, E. Marin, J.R. Macé, M. Cannas, S. Girard, Real time monitoring of water level and temperature in storage fuel pools through optical fibre sensors, Sci. Rep. 7 (1) (2017) 8766, https://doi.org/ 10.1038/s41598-017-08853-7.
- [52] "Luna ODiSI 6000 Data Sheet." https://lunainc.com/sites/default/files/assets/ files/data-sheet/Luna%20ODiSI%206000%20Dat%20Sheet.pdf. Accessed on June 1, 2023.
- [53] W. Meng, M. Valipour, K.H. Khayat, Optimization and performance of cost-effective ultra-high-performance concrete, Mater. Struct. 50 (1) (2017) 29, https://doi.org/10.1617/s11527-016-0896-3.
- [54] ASTM C 157, ASTM International, West Conshohocken, PA, USA, 1999, https://doi.org/10.1520/C0157\_C0157M-99.
- [55] W. Meng, K.H. Khayat, Mechanical properties of ultra-high-performance concrete enhanced with graphite nanoplatelets and carbon nanofibers, Compos. Part B: Eng. 107 (2016) 113–122, https://doi.org/10.1016/j.compositesb.2016.09.069.
- [56] 2020, ASTM C39/C39M-20 (2020). "Standard test method for compressive strength of cylindrical concrete specimens," ASTM International, West Conshohocken, PA, USA. https://doi.org/10.1520/C0039\_C0039M-20.
- [57] 2017, ASTM C496/C496M-17 (2017). "Standard test method for splitting tensile strength of cylindrical concrete specimens," ASTM International, West Conshohocken, PA, USA. https://doi.org/10.1520/C0496\_C0496M-17.

- [58] Ultra-High Performance Concrete. https://www.cement.org/learn/concrete-technology/concrete-design-production/ultra-high-performance-concrete. Accessed on October 8, 2023.
- [59] F. Micelli, A. Renni, A.G. Kandalaft, S. Moro, Chapter 7 Fiber-reinforced concrete and ultrahigh-performance fiber-reinforced concrete materials. New Materials in Civil Engineering, Butterworth-Heinemann, 2020, pp. 273–314, https://doi.org/ 10.1016/B978-0-12-818961-0.00007-7.
- [60] J. Du, W. Meng, K.H. Khayat, Y. Bao, P. Guo, Z. Lyu, A. Abu-Obeidah, H. Nassif, H. Wang, New development of ultra-high-performance concrete (UHPC), Compos. Part B: Eng. 224 (2021) 109220, https://doi.org/10.1016/j. compositesb.2021.109220.
- [61] V. Perry, "What really is ultra-high performance concrete towards a global definition.". Proceedings of the 2nd international conference on UHPC materials and structures, RILEM Publications, Fuzhou, 2018 https://www.researchgate.net/pub-lication/340441896\_What\_Really\_is\_Ultra-High\_Performance\_Concrete\_Towards\_a\_Global\_Definition#fullTextFileContent. Accessed on June 1, 2023.
- [62] S.H. Kwon, S.P. Shah, Prediction of early-age cracking of fiber-reinforced concrete due to restrained shrinkage, Acids Mater. J. 105 (4) (2008) 381–389, https://doi. org/10.14359/19900.
- [63] W. Dong, X. Zhou, Z. Wu, G. Kastiukas, Effects of specimen size on assessment of shrinkage cracking of concrete via elliptical rings: Thin vs. thick, Comput. Struct. 174 (2016) 66–78, https://doi.org/10.1016/j.compstruc.2015.12.005.

- [64] H. Rong, W. Dong, W. Yuan, X. Zhou, An improved ring test to assess cracking resistance of concrete under restrained shrinkage, Theor. Appl. Fract. Mech. 113 (2021) 102976, https://doi.org/10.1016/j.tafmec.2021.102976.
- [65] X. Tan, S. Mahjoubi, X. Zou, W. Meng, Y. Bao, Metaheuristic inverse analysis on interfacial mechanics of distributed fiber optic sensors undergoing interfacial debonding, Mech. Syst. Signal Process. 200 (2023) 110532, https://doi.org/ 10.1016/i.vmssp.2023.110532.
- [66] J.H. Moon, F. Rajabipour, B.J. Pease, J. Weiss, Quantifying the influence of specimen geometry on the results of the restrained ring test, J. ASTM Int. 3 (8) (2006) 1–14, https://doi.org/10.1520/JAI100436.
- [67] D.Y. Yoo, J.J. Park, S.W. Kim, Y.S. Yoon, Influence of ring size on the restrained shrinkage behavior of ultra high performance fiber reinforced concrete, Mater. Struct. 47 (2014) 1161–1174, https://doi.org/10.1617/s11527-013-0119-0.
- [68] J. Tian, X. Wu, X. Tan, W.W. Wang, S. Hu, Y. Du, J. Yuan, W. Huang, X. Huang, Experimental study and analysis model of flexural synergistic effect of reinforced concrete beams strengthened with ECC, Constr. Build. Mater. 352 (2022) 128987, https://doi.org/10.1016/j.conbuildmat.2022.128987.
- [69] J. Feng, S.X. Chua, F. Yang, S. Qian, Crack repairing of high strength engineered cementitious composites using bacteria-free waste medium, Cem. Concr. Compos. 123 (2021) 104203, https://doi.org/10.1016/j.cemconcomp.2021.104203.
- [70] W. Meng, K. Khayat, Effects of saturated lightweight sand content on key characteristics of ultra-high-performance concrete, Cem. Concr. Res. 101 (2017) 46–54, https://doi.org/10.1016/j.cemconres.2017.08.018.